Unique role for lncRNA HOTAIR in defining depot-specific gene expression patterns in human adipose-derived stem cells

Edina Erdos,[1,2,3,4,6] Adeline Divoux,[5,6] Katalin Sandor,[1,2,3,4,6] Laszlo Halasz,[1,2,3,4] Steven R. Smith,[5] and Timothy F. Osborne[1,2,3,4]

[1]Division of Diabetes Endocrinology and Metabolism, [2]Department of Medicine, [3]Department of Biological Chemistry, [4]Department of Pediatrics, Johns Hopkins University School of Medicine; Institute for Fundamental Biomedical Research, Johns Hopkins All Children's Hospital, St. Petersburg, Florida 33701, USA; [5]Translational Research Institute, AdventHealth, Orlando, Florida 32804, USA

Accumulation of fat above the waist is an important risk factor in developing obesity-related comorbidities independently of BMI or total fat mass. Deciphering the gene regulatory programs of the adipose tissue precursor cells within upper body or abdominal (ABD) and lower body or gluteofemoral (GF) depots is important to understand their differential capacity for lipid accumulation, maturation, and disease risk. Previous studies identified the HOX transcript antisense intergenic RNA (HOTAIR) as a GF-specific lncRNA; however, its role in adipose tissue biology is still unclear. Using three different approaches (silencing of HOTAIR in GF human adipose-derived stem cells [GF hASCs], overexpression of HOTAIR in ABD hASCs, and ChIRP-seq) to localize HOTAIR binding in GF hASC chromatin, we found that HOTAIR binds and modulates expression, both positively and negatively, of genes involved in adipose tissue-specific pathways, including adipogenesis. We further demonstrate a direct interaction between HOTAIR and genes with high RNAPII binding in their gene bodies, especially at their 3′ ends or transcription end sites. Computational analysis suggests HOTAIR binds preferentially to the 3′ ends of genes containing predicted strong RNA–RNA interactions with HOTAIR. Together, these results reveal a unique function for HOTAIR in hASC depot-specific regulation of gene expression.

[*Keywords*: fat distribution; subcutaneous adipose tissue; HOTAIR; transcriptome; adipose-derived stem cells; RNAPII; RNA–RNA interaction]

Supplemental material is available for this article.

Received January 19, 2022; revised version accepted May 12, 2022.

Excess adipose tissue accumulation, particularly above the waist, is an important risk factor for all chronic obesity-related diseases, including type 2 diabetes (T2D) (Goodpaster et al. 1997; Duclos 2016). In contrast, adipose tissue accumulation in the subcutaneous gluteal and gluteofemoral (GF) fat depots (below the waist) is relatively protective (Manolopoulos et al. 2010). Upper versus lower body fat expansion varies between individuals of the same sex, age, and BMI. Ethnicity and hormonal balance influence adipose tissue distribution (Goedecke et al. 2009; Isacco et al. 2021); however, the exact molecular mechanisms at the origin of this disparity are still largely unknown.

Preadipocytes and adipose stem cells (ASCs) play an important role in adipose tissue expansion, notably through their proliferation and differentiation into mature adipocytes. Differences between visceral and subcutaneous abdominal (ABD) ASCs have been described (Baglioni et al. 2012); however, there are few reports describing the diversity in ASCs isolated from subcutaneous ABD and GF adipose tissue depots. It is an active area of research in our laboratory, and we recently described their distinct transcriptomic and DNA methylation signatures associated with body shape heterogeneity (Divoux et al. 2021). At the molecular level, the fate of adipogenesis is determined by cell–cell and cell–extracellular matrix (ECM) interactions within the adipose tissue niche (Mor-Yossef Moldovan et al. 2019). Once committed, preadipocytes undergo

[6]**These authors contributed equally to this work.**
Corresponding author: tosborn9@jh.edu
Article published online ahead of print. Article and publication date are online at http://www.genesdev.org/cgi/doi/10.1101/gad.349393.122.

changes in cell shape and movement as part of a highly ordered program of terminal differentiation, where gene regulatory cascades orchestrate the symphonic pattern of gene expression necessary for lipid droplet formation and lipid storage (Rosen and Spiegelman 2000). The coordinated process is governed by gene regulatory programs that involve master transcription factors (TFs; such as PPARγ and C/EBPs) (Morrison and Farmer 1999), along with miRNAs (Shi et al. 2016) and lncRNAs (Squillaro et al. 2020). Advances in the understanding of epigenomic drivers of adipogenesis have also revealed critical roles for chromatin modification and remodeling, as well as DNA methylation (Lee et al. 2019). In this context, our previous work showed that the HOX transcript antisense intergenic RNA (HOTAIR), a GF-specific lncRNA (Karastergiou et al. 2013; Pinnick et al. 2014), is a potential regulator of adipogenesis (Divoux et al. 2014). It has been proposed to function as a scaffold/molecular bridge between PRC2 and LSD1/REST repressor complexes to regulate the chromatin structure of target genes (Tsai et al. 2010; Qu et al. 2019). H3K27 trimethylation and demethylation of H3K4 are mediated by PRC2 and LSD1, respectively, which cocontribute to gene silencing. In addition to its role related to PCR2 and LSD1 repressor complexes, HOTAIR can modify the level of DNA methylation of its targeted genes, but the mechanism is unclear (Bure et al. 2018; Cheng et al. 2018). More recent studies suggested that HOTAIR can also lead to activate gene expression. Notably, its overexpression led to an increase of NF-κB pathway activation (Wang et al. 2021), transcription initiation by RNAPII (Wang et al. 2021), and expression of profibrotic-related genes (Pan et al. 2018). Additionally, expression of genes related to epithelial–mesenchymal transition (EMT) were decreased subsequent to HOTAIR silencing in human pancreatic cells (Tang et al. 2021). However, whether HOTAIR plays a direct or indirect role in situations where its presence corresponds with gene activation is still unknown. Finally, HOTAIR can serve as competitive endogenous RNAs (ceRNAs) at the post-transcriptional regulatory level, mainly by sequestering miRNAs (Liu et al. 2014; Jia et al. 2021). Aberrant expression of HOTAIR in several cancer models is associated with more aggressive disease through gene signatures and cellular phenotypes related to increased proliferation, migration, and metastasis (Gupta et al. 2010). Although some HOTAIR target genes are known (Hajjari and Salavaty 2015), the fact that it is associated with many different cellular functions suggests that additional targets and possible different mechanisms of action remain to be identified. Despite its depot-selective expression being documented in the GF subcutaneous adipose tissue (Karastergiou et al. 2013; Pinnick et al. 2014), its specific role in shaping adipose precursor cell identity remains unclear.

Here, we investigated HOTAIR function in adipose gene regulation by manipulating its expression in human adipose-derived stem cells (hASCs) isolated from ABD versus GF adipose tissue. We used targeted overexpression in the ABD, where HOTAIR expression is normally very low, and knockdown in the GF, where it is significantly expressed, followed by RNA-seq to identify downstream transcriptional targets. Importantly, ABD and GF cells were isolated from the different depots of the same individuals, allowing paired analysis in addition to evaluation of group variation. In parallel, we used ChIRP-seq (Chu et al. 2012) to identify HOTAIR binding sites in GF hASC chromatin. To define the chromatin landscape of the HOTAIR target genes, we performed ATAC-seq profiling coupled with ChIP-seq for several different epigenetic modifications, in addition to RNAPII and CTCF on paired ABD and GF hASCs as well.

Our results provide the first evidence that HOTAIR functions to maintain adipose depot-selective active gene expression via binding to target gene sites preferentially located at transcription end sites (TESs) that are also enriched for RNAPII binding. The HOTAIR TES binding sites correspond to predicted sites of HOTAIR RNA–RNA interaction as well. The coenrichment of RNAPII and HOTAIR together supports a model in which strong HOTAIR-mediated RNA–RNA interactions are involved in its chromatin localization. Additionally, HOTAIR binding at the TES is associated with either an increased or decreased level of gene expression, providing the first direct evidence that HOTAIR binding is associated with both gene activation and repression.

Results

HOTAIR regulates genes related to key depot-specific pathways in hASCs

HOTAIR is one of the most differentially expressed transcripts between GF and ABD hASCs (Divoux et al. 2021), and its role in adipogenesis was suggested by our previous overexpression study (Divoux et al. 2014). Additionally, prior studies in several cancer models have shown that HOTAIR contributes to cell proliferation and migration and ECM remodeling associated with the EMT (Lu et al. 2017; Topel et al. 2020). Because all of these processes contribute to the early phase of adipocyte differentiation, we hypothesized that HOTAIR might play a key role in defining the functional differences between GF and ABD hASCs.

To begin to directly investigate HOTAIR in regulating differences between ABD and GF adipose tissue, we targeted HOTAIR for knockdown in GF-derived hASCs coupled with HOTAIR ectopic overexpression in ABD-derived hASCs. Importantly, the silencing by siRNA resulted in a reduction in HOTAIR expression to the low level naturally observed in ABD cells (Supplemental Fig. S1A, left graph), and the lentivirus-based transfection method resulted in expression of HOTAIR in ABD-derived cells at similar levels to what is normally present in GF cells (Supplemental Fig. S1A, right graph). One subject showed a relative high expression of HOTAIR after overexpression compared with the other subjects (Supplemental Fig. S1A, right graph). However, when we performed a sample-to-sample distance heat map based on gene expression results from the silencing and overexpression experiments, data obtained with subject 1 were well correlated with the rest of our data (Supplemental Fig. S1B).

Therefore, data from all of the subjects were included in the downstream analysis.

Interestingly, the genes that were increased the most by HOTAIR silencing in GF cells are involved in immune responses (*CXCL11*, *CXCL10*, *CCL8*, *ICAM1*, *IDO1*, *BATF2*, *GBP5*, and *RSAD2*), whereas the gene that is most down-regulated is *ROR1*, a mediator of the positive effect of resistin (RETN) on adipogenesis (Fig. 1A; Sánchez-Solana et al. 2012). Conversely, genes that are increased after HOTAIR overexpression in ABD cells are positively associated with adipogenesis (*SFRP2*, *SMOC2*, *CRLF1*, and *COMP*) (Denton et al. 2018), obesity (*ITIH5*) (Anveden et al. 2012), or lipid metabolism (*ACKR3*) (Gencer et al. 2021) (Fig. 1B). We reanalyzed our previous RNA-seq data obtained from 18 paired ABD and GF hASCs (Divoux et al. 2021) and identified that the same pathways described here were also differentially expressed in ABD versus GF hASCs (EMT, TNFα signaling, adipogenesis, p53 pathway, and glycolysis), consistent with HOTAIR playing a major role in the differential expression pattern for ABD versus GF hASCs.

We next compared the set of genes dysregulated by HOTAIR in hASCs and two other published data sets where HOTAIR was silenced in two different cell lines: one derived from human embryonic kidneys and one derived from human breast cancer (see the Materials and Methods). Several pathways were similarly associated with HOTAIR DEGs in our study and the published data sets (Supplemental Fig. S1C). These include EMT, TNFα signaling, cholesterol homeostasis, hypoxia, glycolysis, and p53 pathways. Interestingly, adipogenesis, fatty acid metabolism, and oxidative phosphorylation were dysregulated only in our studies. Notably *CAVIN1*, *CAVIN2*, and *CD36* were down-regulated after HOTAIR silencing in GF hASCs. These three genes are required for lipid droplet formation and fatty acid uptake. These data suggest that HOTAIR contributes to similar transcriptional pathways in cancer and adipose tissue but also has unique roles in

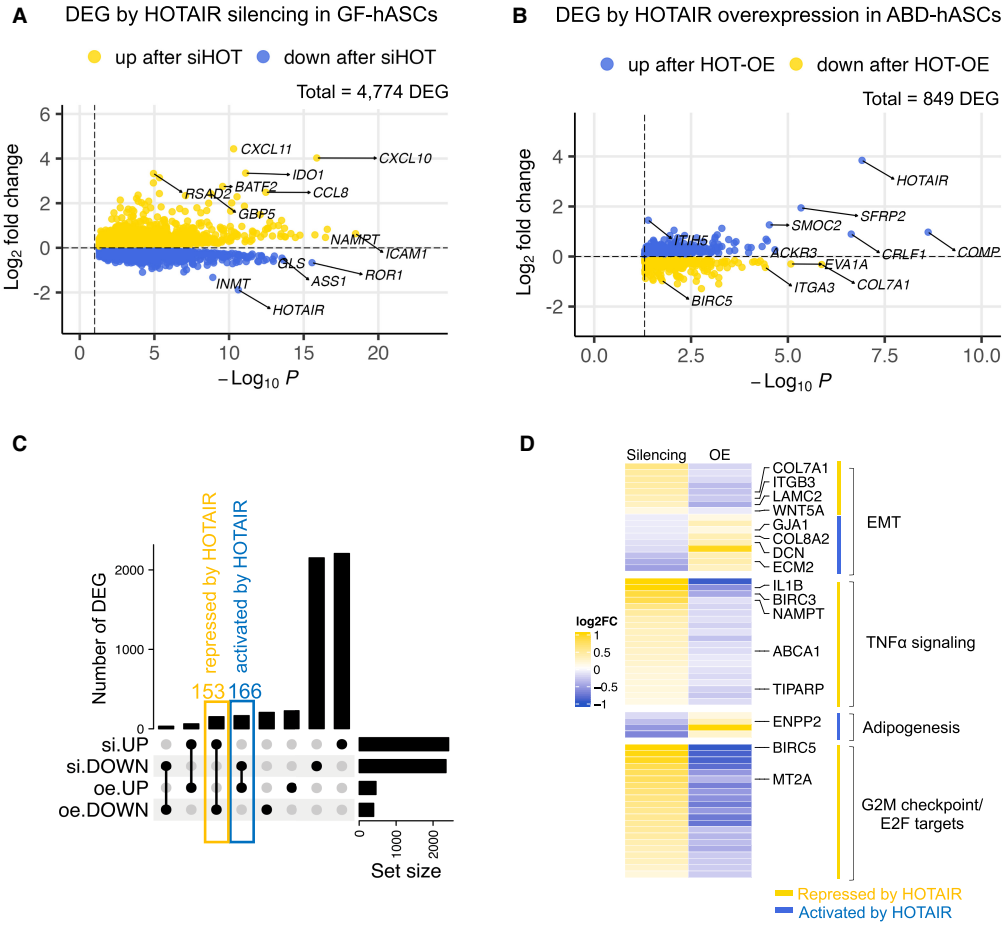

Figure 1. HOTAIR regulates genes related to EMT, TNFα signaling, adipogenesis, and G2M/E2F target pathways in hASCs. (*A*,*B*) Volcano plots show differentially expressed genes (DEGs) after HOTAIR silencing (si) in GF-derived hASCs (*A*) and HOTAIR overexpression (oe) in ABD-derived hASCs (*B*). $N = 4$ subjects, P-value < 0.05. Genes repressed or activated by HOTAIR are colored yellow or blue, respectively. (*C*) UpSet plot showing the common DEGs after HOTAIR silencing in GF hASCs and overexpression in ABD hASCs. (Yellow) Genes repressed by HOTAIR, (blue) genes activated by HOTAIR. (*D*) Heat map representation of the expression levels of genes repressed (yellow) or activated (blue) by HOTAIR associated with epithelial–mesenchymal transition (EMT), TNFα signaling, adipogenesis, and G2M/E2F target pathways. Key genes are highlighted, and a comprehensive list is in Supplemental Table S1.

hASCs, potentially linked to a depot-specific transcriptional signature.

We next defined the genes activated by HOTAIR as those that are increased by overexpression in the ABD and down-regulated by silencing in the GF. Conversely, genes repressed by HOTAIR are defined as those that are down-regulated in the ABD following overexpression and increased in the GF after silencing (Fig. 1C). A large set of genes was positively regulated by HOTAIR in hASCs (n = 166) (Fig. 1C), and pathway analysis revealed that the genes exclusively down-regulated by HOTAIR are significantly associated with the G2/M checkpoint, E2F targets, and the IFNγ response (Fig. 1D; Supplemental Fig. S1C). The genes selectively activated by HOTAIR are associated with adipogenesis (Fig. 1D) and myogenesis (Supplemental Fig. S1C). Intriguingly, HOTAIR seems to repress genes known to inhibit adipogenesis, such as *WNT5A* and *IL1β*, but also *CEBPβ*, a key transcription factor involved in the early phase of preadipocyte differentiation. The effects on genes associated with EMT were mixed (Fig. 1D; Supplemental Fig. S1C). Importantly, most of the genes grouped under the EMT pathway are involved in the cytoskeleton or the extracellular matrix (ECM). Remodeling of both is critical for ASC commitment to the adipocyte lineage (Rosen and MacDougald 2006; Mor-Yossef Moldovan et al. 2019).

HOTAIR binds to transcription end sites of GF hASC genes

To determine whether the effects on gene expression were due to direct or indirect effects of HOTAIR action, we used ChIRP-seq to localize where HOTAIR binds in GF chromatin (see the Materials and Methods; Supplemental Fig. S2A). We identified 36,612 HOTAIR peaks with a wide range of read counts per peak (up to 1339; average reads per kilobase per million [RPKM] = 178). Previous ChIRP-seq studies on HOTAIR suggested it binds mainly to introns in human breast cancer cells (Jarroux et al. 2021). However, we observed >70% of the ChIRP-seq peaks in GF hASCs overlapping with gene bodies (Fig. 2A). Surprisingly, ∼15% were found at the 3′ and transcription termination sites (TTSs or TESs) of the targeted genes (Fig. 2A). Supplemental Figure S2B shows a snapshot of HOTAIR ChIRP-seq peaks at the HOXB locus, a prototypical HOTAIR target locus (Gupta et al. 2010), representative of the different patterns of HOTAIR binding sites around its target genes in GF hASCs.

Motif analysis using the top 10,000 ChIRP-seq peaks ranked by RPKM revealed an enrichment for the Zic1::Zic2 motif and the prototypical GA-rich HOTAIR motif (Fig. 2B; Chu et al. 2011). Less expected, the polyadenylation (polyA) signal sequence motif was significantly enriched in the HOTAIR peak regions. To further explore this specific motif and understand how it is related to HOTAIR binding, we separated the total number of ChIRP-seq peaks into two groups according to the presence or absence of the AATAAA motif. The distribution of this motif through genomic annotation confirmed that the peaks containing the polyA signal sequence were enriched at the 3′ UTRs of genes compared with the peaks without this specific sequence (Fig. 2C, purple on the histogram). However, this analysis also revealed a wider distribution of HOTAIR binding sites containing the AATAAA motif throughout the genome, indicating that HOTAIR binding to this motif is not restricted to the 3′ ends of genes.

Annotation of the ChIRP-seq peaks to the closest gene (as described in the Materials and Methods) revealed that HOTAIR binds to 9289 protein-coding genes. Interestingly, read distribution across the gene body showed an enrichment of HOTAIR binding at gene TESs rather than the transcription start sites (TSSs), as described for HOTAIR in previous studies (Fig. 2D; Li et al. 2021), consistent with our observations in Figure 2A. Pathway analysis using the top 5000 genes with the most HOTAIR peaks ranked by RPKM indicated that HOTAIR binds preferentially to genes involved in EMT, G2/M checkpoint, adipogenesis, known E2F targets, and TNFα signaling via NF-κB (Fig. 2E). Importantly, these are the same gene expression pathways that were affected by silencing and overexpression of HOTAIR in Figure 1. Taken together, these results confirm that HOTAIR has a regulatory effect on specific genes that are involved in pathways related to differential GF versus ABD subcutaneous adipose tissue depot signatures.

Chromatin features of direct and indirect HOTAIR target genes

The combination of RNA-seq analysis for HOTAIR knockdown and overexpression with the genomic localization revealed by ChIRP-seq allowed us to separate the genes affected by HOTAIR into direct and indirect targets of HOTAIR action. Of the 4774 DEGs after HOTAIR silencing in GF hASCs, 3407 (71%) have ChIRP-seq peaks. The same proportion was observed in the HOTAIR overexpression experiment, where 584 (69%) of the 849 DEGs after HOTAIR overexpression have associated HOTAIR binding sites revealed through ChIRP-seq.

To define the chromatin landscape around HOTAIR target genes, we independently used ATAC-seq to probe chromatin openness combined with ChIP-seq to profile H3K4me3, H3K4me2, H3K27ac, H3K27me3, CTCF, and RNAPII binding in chromatin isolated from ABD and GF hASCs cultured from the same four donors used in the HOTAIR silencing and overexpression assays. We integrated and visualized the data using ChromHMM software (Ernst and Kellis 2017). The ChromHMM profiling returned 10 emission states representing different combinations of the individual ChIP-seq/ATAC-seq sites (described in the Materials and Methods; visualized in Supplemental Fig. S3A). Next, we displayed the ChromHMM landscape around the DEGs affected by HOTAIR silencing in GF hASCs (Fig. 3A) and around the DEGs identified by HOTAIR overexpression in ABD hASCs (Supplemental Fig. S3B). We separated the DEGs into those with or without associated HOTAIR ChIRP-seq peaks (Fig. 3A, left and right graphs, respectively; Supplemental Fig. S3B, left and right graphs, respectively). This allowed us to visualize

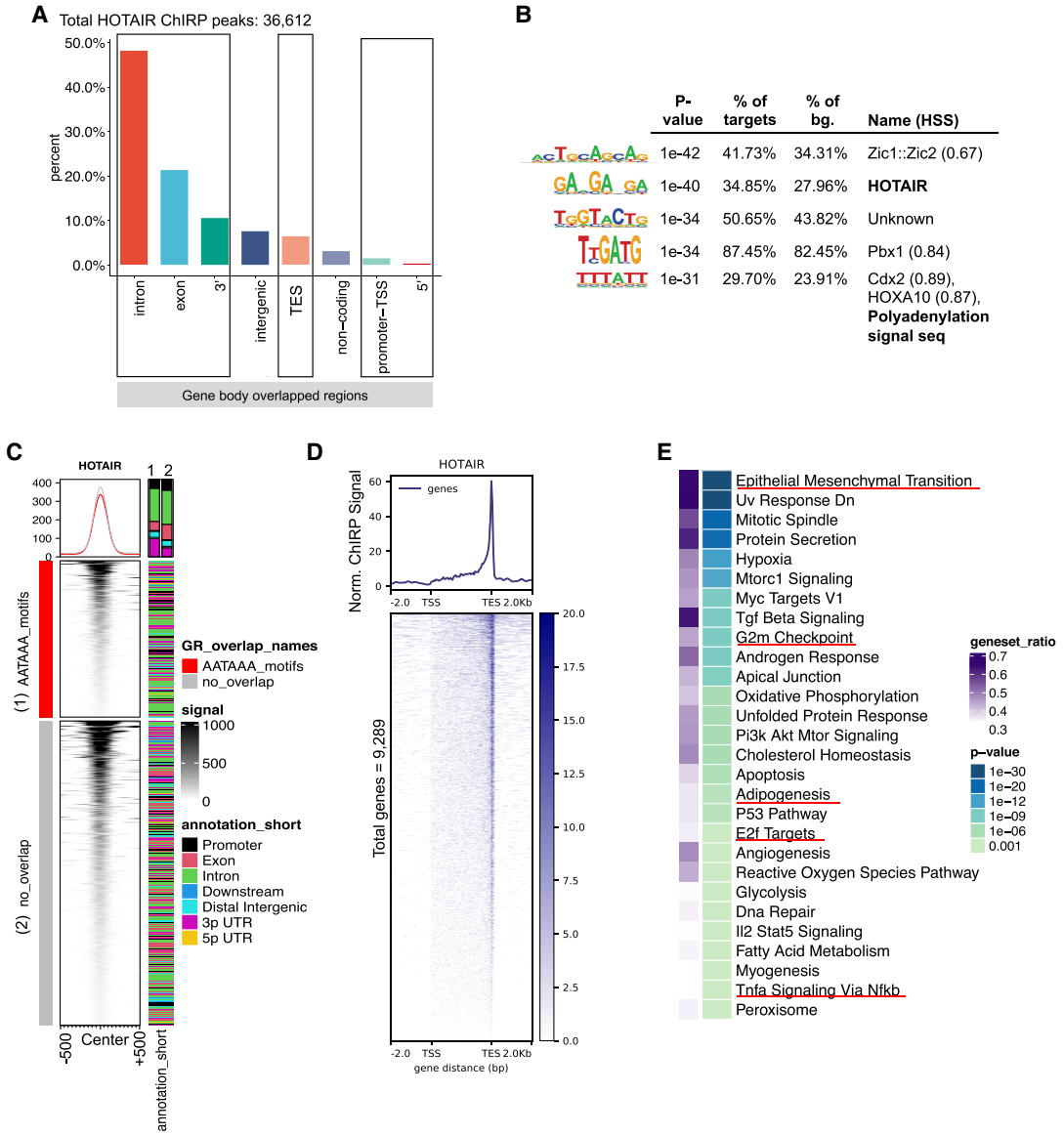

Figure 2. Genomic characterization of HOTAIR ChIRP-seq peaks. (*A*) Bar graph representing the genomic distribution of the 36,612 HOTAIR ChIRP peaks in GF-derived hASCs. (*B*) Motif enrichment analysis for the top 10,000 HOTAIR ChIRP peaks. Enriched motif matrices are presented along with the *P*-value. The percentages of each motif found in the target (% of target) and background (% of bg) genomic regions are indicated. The HOMER similarity score is indicated in parentheses after the name. (*C*) Heat map representation of the read density around the center of HOTAIR ChIRP-seq peaks (±500 bp), with genomic distribution (*right*) grouped by the presence (red, 1) or absence (gray, 2) of the polyadenylation signal motif. (*D*) Heat map showing gene-associated HOTAIR ChIRP-seq signal at gene-coding regions, including 2 kb upstream of TSSs and 2 kb downstream from TESs. (*E*) Plot showing the significant pathways related to the top 5000 genes, with ChIRP-seq peaks ranked by RPKM (reads per kilobase per million). Gene set ratios are represented along with the *P*-value. Pathways with *P*-value < 0.01 are represented.

differences between direct and indirect HOTAIR targets. There were two ChromHMM emission states enriched around the DEGs associated with HOTAIR perturbation, corresponding to "TssA" and "Tx_RNAPII_high_TES" (Fig. 3A; Supplemental Fig. S3B). The TssA state corresponds to an enrichment of all of the tested active histone marks and RNAPII binding at the TSSs (Supplemental Fig. S3A). The second enriched emission state corresponds to high RNAPII binding at the TESs, which was present only in the DEGs that also contain a HOTAIR binding site (Fig. 3A, green arrow; Supplemental Fig. S3B). Figure 3B shows a snapshot of the colocalization of HOTAIR (ChIRP-seq data) with data for RNAPII, H3K4me2, and H3K27me3 around *EGR1* and *IGFB4*. Expression of these two transcripts changed after HOTAIR manipulation. IGFBP4 is a regulator of insulin-like growth factor (IGF) required for proper adipogenesis (Boney et al. 1994) and adipose tissue expansion through effects on adipogenesis (Gealekman

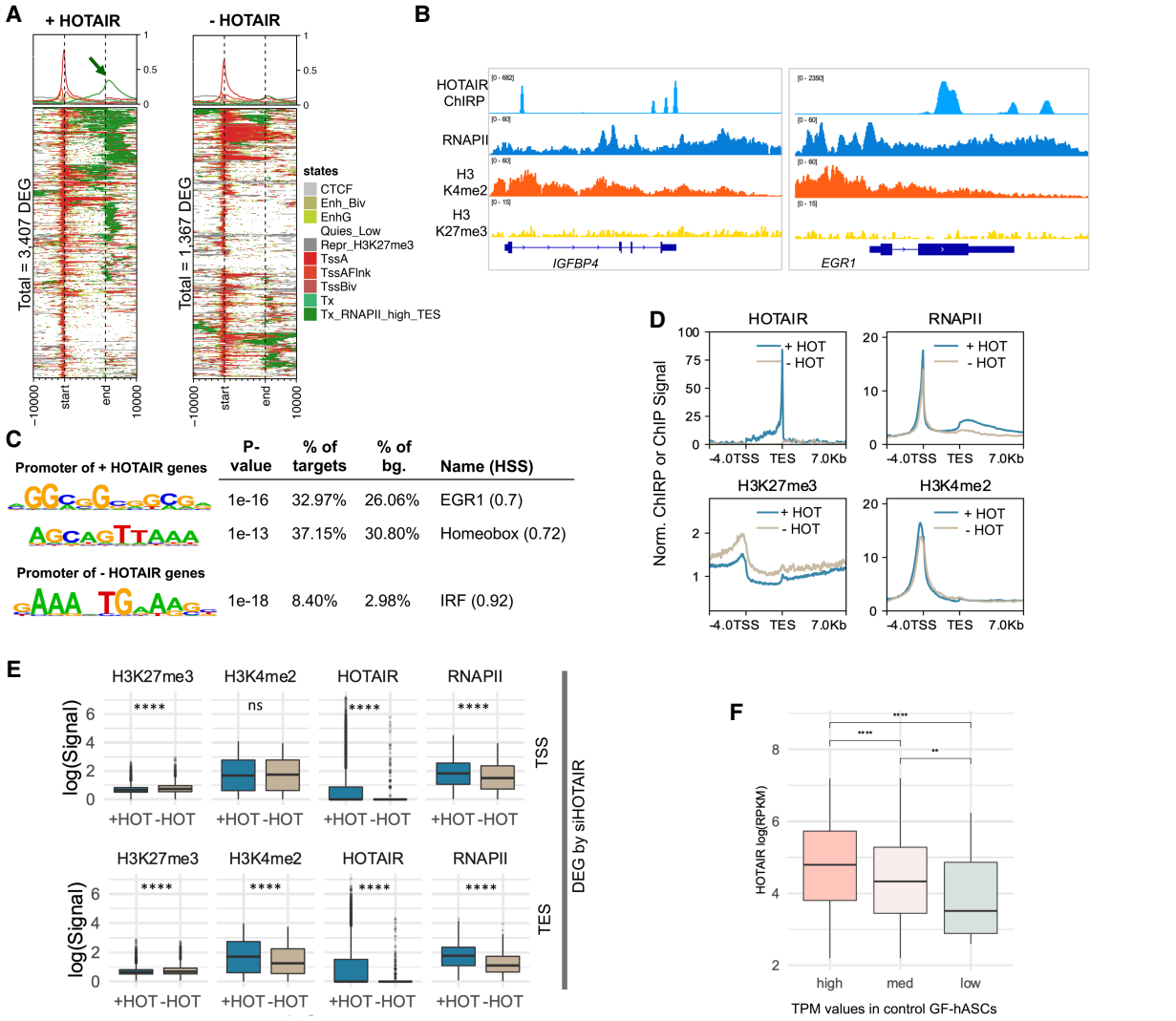

Figure 3. Chromatin features of HOTAIR direct and indirect target genes in GF hASCs. (*A*) ChromHMM heat map representation of data from an independent set of the same four GF hASCs used for the silencing experiment in Figure 1. Signals around the 4774 DEGs after HOTAIR silencing (from Fig. 1A) were analyzed and separated into those with HOTAIR (*left*) or without HOTAIR (*right*) ChIRP-seq peaks in their gene bodies. (Enh-Biv) Enhancer bivalent, (EnhG) enhancer, (Repr) repressed, (TssA) active transcription start site, (TssAFlnk) active transcription start site-flanking regions, (TssBiv) bivalent transcription start site, (Tx) transcription. (*B*) Screenshot showing HOTAIR ChIRP, RNAPII, H3K4me2, and H3K27me3 binding sites at *IGFBP4* and *EGR1* genes in GF hASCs. (*C*) Motif enrichment analysis at the promoters of DEGs after silencing overlapping with (+HOTAIR) or without (–HOTAIR) HOTAIR ChIRP peaks. Enriched motif matrices are presented along with the *P*-value. The percentages of each motif found in the target (% of target) and background (% of bg) genomic regions are indicated. HOMER similarity score is indicated in parentheses after the name. (*D*) Histograms show HOTAIR binding (ChIRP-seq), RNAPII binding, H3K27me3 signal, and H3K2me3 signal (ChIP-seq) around the DEGs from *A*. +HOT or –HOT indicates genes from the *left* or *right* graphs in *A*, respectively. (TES) Transcription end site. (*E*) Box plots show H3K27me3, H3K4me2, RNAPII ChIP-seq, and HOTAIR ChIRP-seq average read densities around the TSSs (*top*) or TESs (*bottom*) of the DEGs from *B*. Unpaired two-sample Wilcoxon test. (****) *P*-value < 0.0001, (ns) not significant. (TSS) Transcription start site, (TES) transcription end site. (*F*) Box plots represent the HOTAIR RPKM from the ChIRP-seq (*Y*-axis) of genes relative to their expression level (*X*-axis), separated into three quantiles representing overall high, medium, or low expression in control GF hASCs. $N = 4$. Data for the DEGs affected by HOTAIR silencing from Figure 1 are represented. Unpaired two-sample Wilcoxon test. (****) *P*-value < 0.0001, (**) *P*-value < 0.01.

et al. 2014). Inversely, EGR1 inhibits adipogenesis, but the mechanism remains to be determined (Boyle et al. 2009). Interestingly, motif analysis revealed an enrichment of the EGR1 motif at the promoters of the 3407 DEGs after HOTAIR silencing that also contain HOTAIR binding sites (Fig. 3C).

To look deeper into the observations revealed by ChromHMM and to quantify the individual histone marks and RNAPII binding around the HOTAIR-associated DEGs that contain or lack ChIRP-seq peaks, we separately evaluated the read densities for RNAPII, H3K4me2, and H3K27me3 ChIP-seq (Fig. 3D; Supplemental Fig. S3C).

This confirmed that HOTAIR and RNAPII are reciprocally localized at the TSSs and the TESs of DEGs following silencing of HOTAIR in GF hASCs (Fig. 3D) or overexpression in ABD hASCs (Supplemental Fig. S3D). In contrast, we observed an inverse binding level between HOTAIR and H3K27me3 at the total set of HOTAIR-bound target genes (Fig. 3D,E; Supplemental Fig. S3C,D).

To further investigate the relationship between HOTAIR binding and gene expression, we grouped the genes that were differentially expressed following HOTAIR silencing into tertiles based on their expression level (high, medium, and low), reflected by transcripts per million (TPM) values from the RNA-seq study in control GF cells (Fig. 3F). The results show that highly expressed genes have more robust binding of HOTAIR, consistent with the model that HOTAIR binding is related to gene activity.

hASC depot-specific genes are associated with HOTAIR regulation and differential RNAPII binding

Since HOTAIR is a GF-specific transcript, we aimed to determine whether its genomic localization was associated with differential RNAPII binding between ABD and GF hASCs. We used diffBind around the genes with ChIRP-seq peaks to compare RNAPII binding on chromatin isolated from ABD versus GF hASCs in the same data set analyzed above. We identified 208 genes with depot-specific RNAPII gene density through their coding sequences (140 ABD-specific and 68 GF-specific). As shown in Figure 4A, *IRS2*, *DHRS3*, and *COL4A1* genes displayed the most ABD-specific RNAPII signal in their coding sequences, whereas *ZIC1*, *HOXC11*, and *HOTAIR* have the most GF-specific RNAPII binding signals. Next, we compared the chromatin features revealed through our ChromHMM analysis around these genes (Supplemental Fig. S4A). The ABD-enriched genes showed ChromHMM states corresponding to active transcription around the TSSs and TESs in both ABD- and GF-derived hASCs, while GF-specific genes showed higher RNAPII binding at TESs in GF hASC chromatin compared with ABD hASC chromatin (Supplemental Fig. S4A, green arrow). We next compared the average HOTAIR peak density (RPKM) in GF hASCs between the ABD- or GF-specific genes (defined by RNAPII diffBind analysis). The GF-specific genes had a significantly higher association of HOTAIR than the ABD-specific genes (Fig. 4B).

As a next step, we evaluated how many genes that were affected by HOTAIR perturbation were also associated with differential RNAPII binding between ABD and GF hASCs. We identified a total of 28 genes, 12 of which were activated by HOTAIR (decreased following knockdown of HOTAIR and increased following HOTAIR overexpression), while nine have more RNAPII binding in GF cells compared with ABD cells (Fig. 4C, top of the heat map). Inversely, among the 10 genes repressed by HOTAIR (increased following HOTAIR knockdown and decreased following HOTAIR overexpression), seven had more RNAPII binding in ABD compared with GF hASCs (Fig. 4C, bottom of the heat map). The remaining six genes have conflicting patterns following HOTAIR silencing or overexpression, suggesting a more complex regulatory mechanism. ChromHMM representation around the 28 genes regulated by HOTAIR highlighted an enrichment of RNAPII binding at their TESs in the GF cells compared with the ABD cells (Supplemental Fig. S4B, green arrow).

Next, we examined the expression level of the genes altered by HOTAIR manipulation in the RNA-seq data from our previous study mentioned above that included a comparison of ABD hASC versus GF hASC gene expression in 18 women (Divoux et al. 2021). Expression of *ABCA1* was repressed by HOTAIR in the present study and, consistent with this pattern, was also expressed at a lower level in our previous report (Fig. 4D,E). *ENPP2* and *THRB* were both activated by HOTAIR (Fig. 4C) and, consistent with this response, were both expressed at higher levels in our GF RNA-seq data (Fig. 4D,E). Interestingly, adipocyte-specific knockout of *ENPP2* in mice reduced adipocyte size in different fat depots (Nishimura et al. 2014). Taken together, these data suggest that HOTAIR binding is associated with increased RNAPII binding in GF-derived hASCs, notably at target gene TESs. Thus, overall, our study suggests that HOTAIR plays a meaningful role in the different patterns of gene expression in ABD versus GF adipose depots.

Higher predicted RNA–RNA interactions between HOTAIR and transcripts at TES chromatin

Previous studies have shown that HOTAIR interacts with chromatin via RNA–RNA interactions (Meredith et al. 2016; Balas et al. 2021). In these studies, the genome-wide HOTAIR-dependent localization of PRC2 activity occurs at loci where the encoded transcripts are predicted to make more favorable RNA–RNA interactions with HOTAIR (Meredith et al. 2016; Balas et al. 2021). Thus, we compared how our ChIRP-seq data for HOTAIR intersect with the transcriptome-wide location of the predicted HOTAIR RNA–RNA interaction sites (see the Materials and Methods). With a threshold of a minimal free energy cutoff of –24.5 kcal/mol, there were 12,719 predicted RNA–RNA interactions between HOTAIR and other genome-wide transcripts. We then intersected the list of these RNA–RNA interactions with our ChIRP-seq data set. Thirty-four percent (4300) overlap with genes containing HOTAIR ChIRP-seq peaks (Supplemental Fig. S5). Interestingly, there was a higher frequency of these predicted sites of high-energy RNA–RNA interactions in the gene bodies of mRNA-encoding genes that contain HOTAIR ChIRP-seq peaks, and most notably at their TESs (Fig. 5A, blue bars). In contrast, transcripts without HOTAIR ChIRP-seq peaks were enriched in non-mRNA-containing transcripts (Fig. 5A, beige bars). In addition, a comparison of the free energy sum of RNA–RNA interactions between mRNAs with (+HOT) and without (−HOT) HOTAIR ChIRP-seq peaks revealed stronger predicted interactions with HOTAIR mRNA targets than non-HOTAIR targets, independent of the location of HOTAIR binding within the coding sequence (Fig. 5B). In contrast, there was no difference in binding energy for non-mRNA transcripts with or without HOTAIR (Fig. 5B). This suggests that HOTAIR is

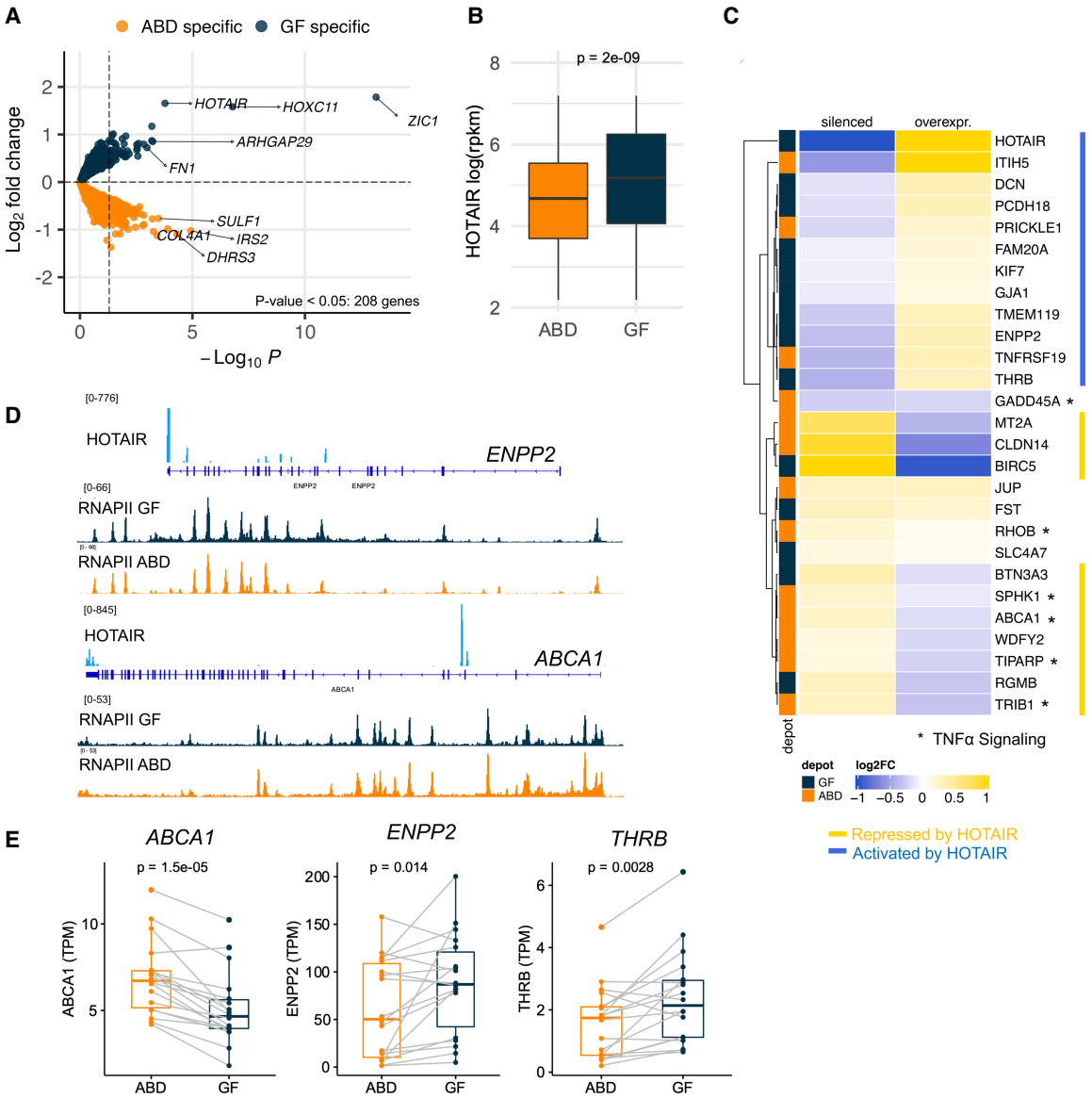

Figure 4. Key genes associated with HOTAIR regulation and differential RNAPII binding between ABD (orange) and GF (dark blue) hASCs. (*A*) Volcano plot representing the 208 genes with HOTAIR ChIRP-seq peaks and differential RNAPII bindings between ABD hASCs and GF hASCs. $P < 0.05$. (*B*) Box plot showing the HOTAIR RPKM at genes with differential RNAPII binding between ABD and GF hASCs. $N = 4$ subjects. Unpaired two-sample Wilcoxon test was used for statistical analysis. (ABD) ABD-RNAPII binding-specific genes, (GF) GF-RNAPII binding-specific genes. (*C*) Heat map showing DEGs affected by HOTAIR (silencing or overexpression from Fig. 1) associated with differential RNAPII binding between ABD (orange) and GF (dark blue) hASCs. An asterisk marks genes involved in the TNFα signaling pathway at $P = 0.0074$. (*D*) IGV genome browser view of HOTAIR ChIRP-seq peaks in GF hASCs (light blue) and RNAPII peaks in GF (dark blue) and ABD hASCs (orange) around *ENPP2* and *ABCA1* genes. (*E*) Box plots depict *ABCA1*, *ENPP2*, and *THRB* expression levels in ABD and GF hASCs in each subject based on RNA-seq data. $N = 18$ subjects. Paired-sample Wilcoxon tests were used for statistical analysis. Lines are drawn connecting values from ABD versus GF hASCs from the same individual.

preferentially localized at target gene 3′ UTRs associated chromatin through RNA–RNA base pair interactions with the encoded gene transcript.

To further explore the role of predicted HOTAIR–RNA interactions, we analyzed ChIP-seq read densities through genes with predicted RNA–RNA interactions within their 3′ UTRs grouped by the presence of HOTAIR ChIRP-seq peaks in the gene bodies. This comparison revealed enrichment of RNAPII binding at the TSSs and a broader RNAPII-enriched peak at the TESs of HOTAIR-bound genes, along with a broad decrease of gene-associated H3K27me3 (Fig. 5C). High H3K4me2 enrichment was also observed around TSSs of HOTAIR-bound genes (Fig. 5C).

These results suggest that HOTAIR participates in an active regulatory mechanism via RNA–RNA interactions located at target gene 3′ UTRs. To validate this

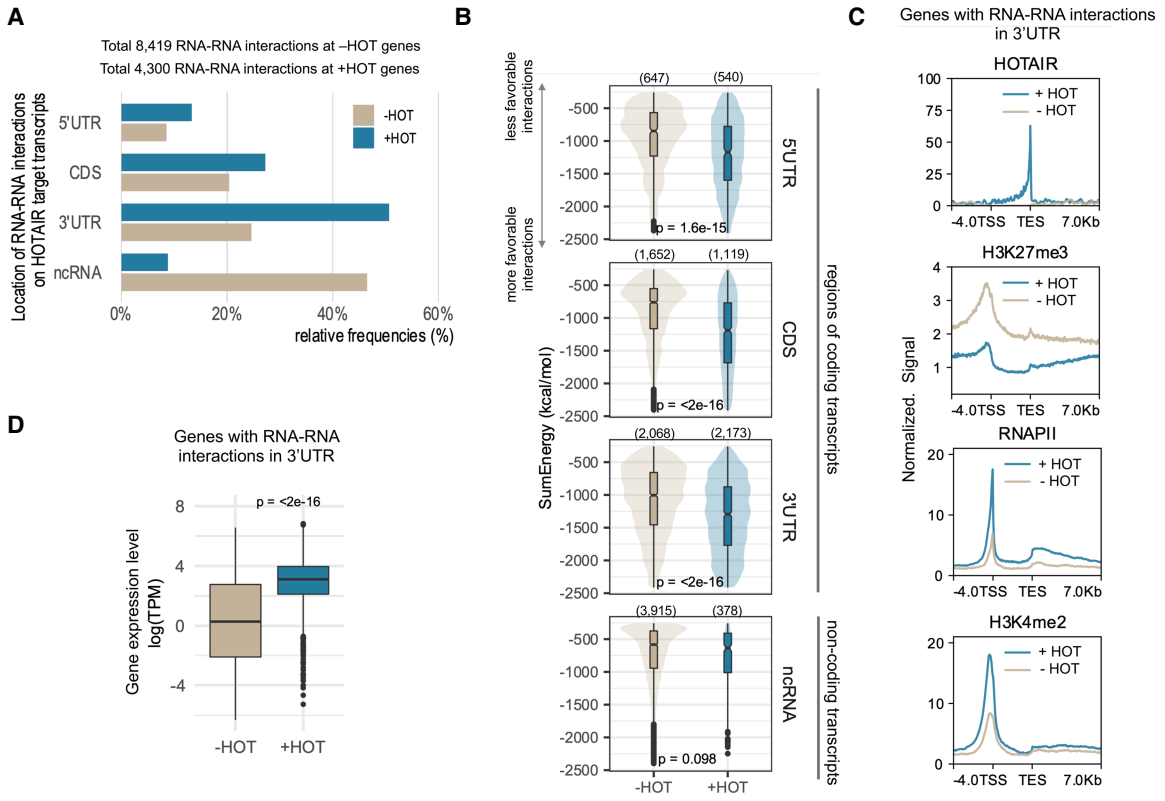

Figure 5. Genes associated with RNA–RNA interactions in 3′ UTRs overlap with presence of HOTAIR ChIRP peaks. (*A*) Bar graphs show the location of RNA–RNA interactions between HOTAIR and the full transcriptome. +HOT or –HOT indicates genes with or without HOTAIR ChIRP-seq peaks, respectively. (UTR5) Untranslated region on the 5′ side, (UTR3) untranslated region on the 3′ side, (ncRNA) noncoding RNA, (CDS) coding sequence. (*B*) Violin plots show the sum of the local interaction energies (SumEnergy) between HOTAIR and other RNA based on the location of predicted interactions. Differences are shown between genes with HOTAIR (+HOT) or without HOTAIR (–HOT) ChIRP signals. Unpaired two-sample Wilcoxon test was used. (*C*) Histograms represent the normalized HOTAIR ChIRP-seq, RNAPII, H3K27me3, and H3K4me2 ChIP-seq signals around genes with predicted RNA–RNA interactions in 3′ UTRs in control GF hASCs. (*D*) Box plot showing the expression level of genes with predicted RNA–RNA interactions in 3′ UTRs in control GF hASCs. $N = 4$. +HOT or –HOT indicates genes with or without HOTAIR ChIRP-seq peaks, respectively. Unpaired two-sample Wilcoxon test was used.

hypothesis, we compared the expression levels of genes with predicted RNA–RNA interactions at their 3′ UTRs and separated them into those with or without HOTAIR ChIRP-seq peaks (Fig. 5D). This comparison showed that the genes bound by HOTAIR were expressed at significantly higher levels than the genes without HOTAIR ChIRP-seq peaks.

hnRNPA2B1 is a potential RNA matchmaker for HOTAIR in GF-derived hASCs

Meredith et al. (2016) identified heterogeneous nuclear riboprotein A2/B1 (hnRNPA2B1) as an interacting partner for HOTAIR and proposed a "matchmaker" model for hnRNPA2B1-mediated targeting of HOTAIR to chromatin. To identify whether a similar mechanism might occur in GF hASCs, we first compared the list of genes whose expression changed after hnRNPA2B1 silencing in a previous study in HEK293T cells (Fig. 6A; Huelga et al. 2012) with the 4774 DEGs affected by HOTAIR silencing in our present study (Fig. 1A). Around 35% of the target genes were common between both experiments (Fig. 6B, Venn diagram), and 75% of them also had HOTAIR ChIRP-seq peaks (Fig. 6B, histogram). These data suggest a broad role for the combined action of hnRNPA2B1 with HOTAIR in transcriptional regulation. To further study the specificity of this interaction in hASCs, we performed hnRNPA2B1 ChIP-seq on the same four GF hASC samples used for HOTAIR silencing. This analysis showed hnRNPA2B1 binding was associated with RNAPII enrichment (Supplemental Fig. S6A); furthermore, this was differentially associated with GF-specific RNAPII binding on hASC chromatin (relative to ABD RNAPII binding) (Supplemental Fig. S6B). Interestingly, the read density for hnRNPA2B1 was also much higher through genes that also contained HOTAIR binding sites, consistent with HOTAIR and hnRNPA2B1 working together to regulate gene activity (Fig. 6C, blue lane vs. brown lane). An example of the binding enrichment patterns for HOTAIR, hnRNPA2B1, and RNAPII at specific genes is provided by the IGV snapshot for the *COL1A1* locus in Figure 6D. Interestingly and independently, genes

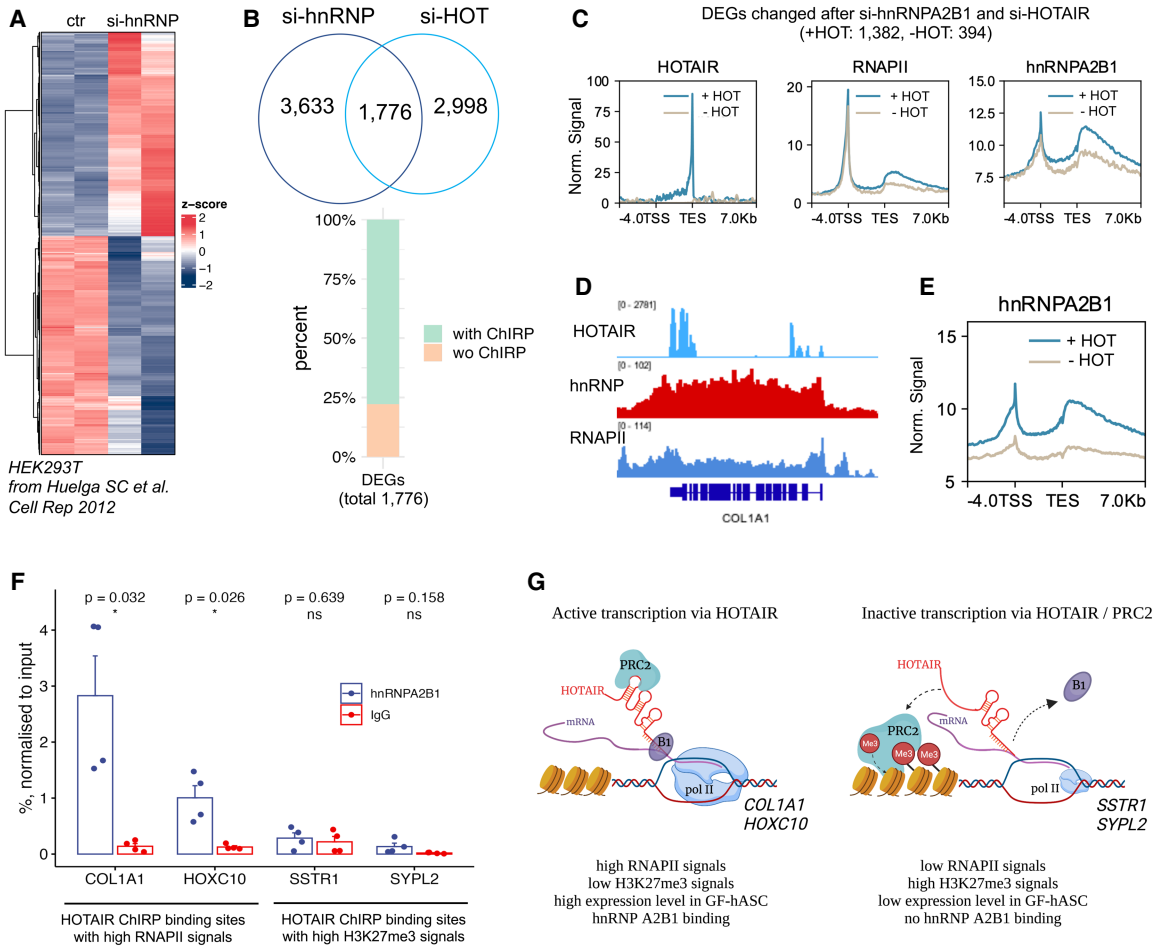

Figure 6. Regulatory mechanisms of HOTAIR lncRNA with hnRNPA2B1 in adipose-derived stem cells. (*A*) Heat map showing 5409 differentially expressed genes after silencing hnRNPA2B1 (si-hnRNP) in HEK293T cells (raw data from Huelga et al. 2012). (*B*) Venn diagram showing the number of unique and common DEGs after hnRNPA2B1 silencing in HEK293T and after HOTAIR silencing in GF hASCs. The bar graph shows the percentage of common DEGs with or without HOTAIR ChIRP peaks. (*C*) Histograms represent the normalized HOTAIR ChIRP-seq, RNAPII, and hnRNPA2B1 ChIP-seq signals around common DEGs after hnRNPA2B1 and HOTAIR silencing. Differences are shown between DEGs with HOTAIR (+HOT) and without HOTAIR (–HOT) ChIRP signals. (*D*) Screenshot showing HOTAIR ChIRP, hnRNPA2B1, and RNAPII ChIP-seq signals at the *COL1A1* gene in GF hASCs. (*E*) Histograms represent the normalized hnRNPA2B1 ChIP-seq signals around genes with predicted RNA–RNA interactions in 3′ UTRs in GF hASCs from Figure 5. Differences are shown between DEGs with HOTAIR (+HOT) and without HOTAIR (–HOT) ChIRP signals. (*F*) Bar graph showing ChIP-qPCR for hnRNPA2B1 binding at DEGs after HOTAIR silencing with HOTAIR ChIRP binding sites in 3′ UTRs from four GF hASCs. $N = 4$. IgG was used as control. Unpaired *t*-test was used. $P < 0.05$ was significant. (*G*) Schematic representation of one of the potential HOTAIR lncRNA-mediated gene expressions with the "matchmaker" hnRNPA2B1 protein. In this model, HOTAIR recognizes chromatin by binding to the nascent mRNA.

with predicted high-energy RNA–RNA interactions between HOTAIR and their 3′ UTRs were enriched for hnRNPA2B1 complex binding compared with the genes without predicted HOTAIR RNA interactions (Fig. 6E). This provides further support for the association of HOTAIR RNA–RNA interactions being at least partially influenced by the cobinding of hnRNPA2B1.

In a follow-up report from the same group, using cross-linking and immunoprecipitation (CLIP) combined with chemical reactivity probing of the HOTAIR secondary structure, the investigators proposed that hnRNPA2B1 association altered the HOTAIR secondary structure and fixed HOTAIR in a conformation that interacts strongly with PRC2 (Balas et al. 2021). The model predicts that in the absence of hnRNPA2B1, HOTAIR adopts an alternative secondary structure that favors PRC2 dissociation, leading to PRC2 deposition within local chromatin to generate the H3K27me3 repression mark (Balas et al. 2021). We hypothesized that the two alternative modes of HOTAIR chromatin association predicted by this model, which are dependent on the presence or absence of colocalized hnRNPA2B1, might explain how HOTAIR binding is associated with gene activation or repression in hASCs. To test this hypothesis, we scanned our data sets and identified *COL1A1* and *HOXC10* as HOTAIR target genes that contained low levels of H3K27me3 and high

levels of RNAPII (Supplemental Fig. S6C). Conversely, we identified *SSTR1* and *SYPL2* as HOTAIR target genes that contained high levels of H3K27me3 located close to the HOTAIR binding sites in their 3′ ends and low levels of RNAPII (Supplemental Fig. S6C). Importantly, these genes were differentially expressed in GF hASCs: *COL1A1* and *HOXC10* were more highly expressed in GF cells, and *SSTR1* and *SYPL2* show the opposite pattern. Consistent with our prediction, ChIP-qPCR showed hnRNPA2B1 enrichment at the *COL1A1* and *HOXC10* loci close to their TES-localized HOTAIR binding sites, whereas the corresponding HOTAIR binding regions at the *SSTR1* and *SYPL2* loci displayed very low levels of hnRNPA2B1 coassociation (Fig. 6F).

Altogether, these data provide evidence that hnRNPA2B1 is an important regulatory partner for HOTAIR in hASCs.

Discussion

The most frequently reported differences in gene expression between upper and lower body adipose depots are genes encoded at the HOXA and HOXC loci on chromosomes 7 and 12, respectively (Karastergiou et al. 2013; Pinnick et al. 2014; Passaro et al. 2017). The HOXC locus encodes the lncRNA HOTAIR, which is expressed at much higher levels in both GF adipose tissue and GF-derived hASCs relative to their ABD-derived counterparts (Divoux et al. 2014). In a previous study, our laboratory showed that supraphysiologic overexpression of HOTAIR in ABD hASCs resulted in more robust adipogenic capacity (Divoux et al. 2014). Here, we investigated the role of HOTAIR in hASCs by inhibiting its expression in the GF through a targeted siRNA approach combined with overexpression in ABD-derived cells. Importantly, the levels of HOTAIR manipulation achieved were much closer to the natural variation observed between ABD and GF cells. The results from both approaches yielded similar sets of HOTAIR target genes. Comparative RNA-seq analyses showed the major genes affected were associated with cell cycle regulation (E2F targets and G2M checkpoint), epithelial-to-mesenchymal transition (EMT), TNFα signaling, and adipogenesis (Supplemental Fig. S1); all these pathways are involved in lipid accumulation in preadipocytes (Farmer 2006; Tzanavari et al. 2010). Similar pathways were revealed in our recent report that compared genes that were differentially expressed between GF- and ABD-derived stem cells (Divoux et al. 2021). Interestingly, down-regulation of HOTAIR in GF hASCs led to an increase of inflammatory marker genes, suggesting that HOTAIR maintains a favorable environment for excess calorie-driven healthy adipose tissue expansion in the GF depot by maintaining a low level of inflammatory pathway activation. Taken together, these results reveal that HOTAIR is associated with beneficial lipid accumulation in the GF depot.

It is noteworthy that gene expression pathways associated with HOTAIR knockdown and overexpression in two other cell models exhibit a significant overlap with our results (Supplemental Fig. S1). However, there are a few interesting pathways that were unique to the different settings. These include Wntβ-catenin and KRAS signaling pathways that were unique to cancer, whereas fatty acid metabolism and oxidative phosphorylation were uniquely enriched in our adipose tissue data. This suggests that HOTAIR regulates a core set of common processes in different cell types but also contributes to critical cell type-specific functions in different physiological settings. A common pathway between the different settings is EMT (Supplemental Fig. S1C). We observed a mixed effect of HOTAIR on EMT-related genes. Interestingly, this was similar to at least one report for HOTAIR in cancer (Jarroux et al. 2021). In our study, most of the genes included in the EMT pathway were associated with the ECM, where remodeling is necessary during early stages of adipogenic differentiation to support the changes required to move from stellar stem cells to round adipocytes (Mor-Yossef Moldovan et al. 2019). The motif analysis using the list of DEGs affected by HOTAIR silencing highlighted enrichment of EGR1 and IRF motifs, and it is noteworthy that these two transcription factors play a role during the early phase of ASC differentiation (Eguchi et al. 2008; Boyle et al. 2009). A recent single-cell RNA-seq study identified a subpopulation of hASCs more primitive than the other cells, characterized by high expression of *DPP4*, and another subpopulation of committed preadipocytes expressing higher levels of *ICAM1* (Merrick et al. 2019). Interestingly, HOTAIR silencing in GF hASCs in our study increased expression of these two markers (P-value < 0.01; log FC 0.12 and 0.63, respectively), suggesting that HOTAIR may be involved in determining the fate of unique hASC subtypes.

Our ChIRP-seq data identified a unique pattern for HOTAIR binding to gene 3′ ends or TESs that was not observed in previous studies of HOTAIR genome-wide localization (Chu et al. 2011). When we combined this with our ChromHMM analysis, we uncovered that HOTAIR binding at target gene TESs is associated with high levels of binding of the elongating form of RNAPII. This suggests that HOTAIR might be targeted to genes that are being actively transcribed. We also showed that HOTAIR binding is positively associated with gene expression levels (Figs. 3F, 4E). This is interesting because Meredith et al. (2016) proposed a model in which HOTAIR might be targeted to genomic sites in chromatin through RNA–RNA base pairing with target sites through a "matchmaker" mechanism. In the same study, ChIRP-MS revealed that HOTAIR interacts with the canonical splicing factor hnRNPA2B1 and that it stabilized RNA–RNA interactions between HOTAIR and its target sites. Our hnRNPA2B1 ChIP-seq in GF ASCs confirmed the strong association between HOTAIR and hnRNPA2B1, in particular for the genes with high predicted site RNA–RNA interactions at their 3′ UTRs.

Meredith et al. (2016) showed that hnRNPA2B1 also favored a unique secondary structure for HOTAIR that interacts favorably with PRC2. This model is consistent with there being different classes of HOTAIR target genes associated with different HOTAIR conformations: one where hnRNPA2B1 is present with high RNAPII and low levels of H3K27me3, and one where hnRNPA2B1 is not present

and there is a low level of RNAPII but a high level of H3K27me3. We found candidate genes of both types in our genomic data sets and showed that they differentially associated with hnRNPA2B1 by ChIP-qPCR (Fig. 6F), as predicted by the model. Importantly, the genes with high level of hnRNPA2B1 binding are highly expressed in GF hASCs, whereas the genes with low hnRNPA2B1 are expressed at higher levels in ABD cells, which is also consistent with the depot-specific roles for HOTAIR. These results suggest that hnRNPA2A2B1 and HOTAIR could interact to modify the GF hASC chromatin landscape, as depicted by the diagram in Figure 6G. This model predicts gene expression differences according to whether hnRNPA2B1 is associated with HOTAIR: When hnRNPA2B1 is not associated, HOTAIR conformation changes, allowing PRC2 to bind to the nearby chromatin, resulting in a high level of H3K27me3 and gene repression. Inversely, when hnRNPA2B1 is associated with HOTAIR, its conformation favors PRC2 binding to HOTAIR rather than to chromatin. Upon dissociation of hnRNPA2B1, HOTAIR is predicted to adopt a conformation that is less favorable for PRC2 interaction, which allows PRC2 to be deposited on nearby chromatin. Our present study provides a significant extension of this in vitro model proposed by Balas et al. (2021), and future investigations are required to test this model further.

Our studies are consistent with HOTAIR playing a significant role in defining the GF versus ABD gene expression profiles in hASCs through binding specifically to chromatin via RNA–RNA interactions with the 3′ ends of nascent target gene transcripts. However, in contrast to histone modifications, which often broadly occupy certain genomic elements, HOTAIR binding sites are focal, specific, and numerous. This observation suggests that HOTAIR occupancy, at least at some sites, more resembles transcription factors, binding directly to DNA. In addition, there are many predicted HOTAIR target genes in our study that do not have HOTAIR binding sites at their TESs and others that do not contain HOTAIR-associated binding sites at all. This highlights that HOTAIR likely regulates gene expression through other direct as well as indirect mechanisms. Indeed, this is supported by previous evidence that HOTAIR also interacts with additional proteins to regulate gene expression (Li et al. 2021) and may also act as a miRNA sponge in multiple settings (Mozdarani et al. 2020).

Materials and methods

Participants and tissue collection

The method of recruitment and the clinical and biochemical parameters of subjects were presented by Divoux et al. (2020). Briefly, paired abdominal and gluteofemoral subcutaneous WAT samples were obtained from 18 healthy premenopausal, weight-stable females. Ten women displayed lower-body adiposity, characterized by a waist to hip ratio (WHR) of <0.78 (pear group; age 33 yr ± 7.2 yr; BMI 28.0 kg/m^2 ± 2.8 kg/m^2), and eight women displayed upper-body adiposity, characterized by a WHR of >0.85 (apple group; age 35 yr ± 6.3 yr; BMI 28.5 kg/m^2 ± 3.5 kg/m^2). All procedures were performed under a research protocol approved by the AdventHealth Institutional Review Board.

Isolation of human adipose-derived stem cells and in vitro experiments

Stromal–vascular fractions (SVFs) were isolated by collagenase digestion of the abdominal and gluteofemoral subcutaneous adipose tissues. SVFs were plated and grown in proliferation medium containing 2.5% FBS, FGF, and EGF. Human adipose-derived stem cell (hASC) populations were enriched as previously described (Divoux et al. 2021). Briefly, the cells presenting the endothelial marker CD31 at their surface were removed by magnetic beads. For HOTAIR overexpression, down-regulation, and ChIP-seq studies, we used cultured ASCs obtained from four subjects randomly selected (age 37 yr ± 7.5 yr, BMI 29.7 kg/m^2 ± 2.0 kg/m^2).

Transfection of hASCs

HOTAIR lentivirus was produced following the LentiX tetOne inducible expression system protocol (Clontech 631844 and 631847); the pLVX tetOne puro luciferase system was used as control. It was generated by cotransfection of HEK293 packaging cells with pLVX-tetOne-HOTAIR-Puro plasmid or control plasmid and packing mix (packaging vector psPAX or pMD2.G). The virus was titrated with the qPCR lentivirus titer kit (AbmGood LV900). The all-in-one pLVX-TetOne-Puro vector expressed the Tet-On 3G transactivator from the constitutive human PGK promoter in the forward orientation and HOTAIR from the PTRE3GS promoter in the reverse orientation. In the presence of doxycycline, the Tet-On 3G transactivator specifically bound and activated high-level transcription from the inducible promoter that controls HOTAIR expression. HOTAIR and control lentiviruses were transfected into ABD hASCs for 48 h at MOI = 10. Four days later, transfected cells were selected with 1 ug/mL puromycin for 2 wk. Cells were collected and seeded in six-well plates overnight, and 100 ng/mL doxycycline was added. Cells were harvested 24 h later for RNA extraction using RNeasy kit (Qiagen). Overexpression was validated by RT-qPCR as described by Roqueta-Rivera et al. (2016) (normalized by PPIA). Overexpression was made twice in four independent cells; two originated from apple-shaped women, and two originated from pear-shaped women.

HOTAIR silencing via siRNA transfection

GF hASCs were seeded in 12-well plates. Seven hours later, 400 nM HOTAIR siRNA (lincode human HOTAIR siRNA, SMARTPool, Dharmacon) or negative control (lincode nontargeting pool, Dharmacon) was transfected into hASCs using DharmaFECT transfection reagent (Dharmacon) according to the company's protocol for 72 h. At the end of the transfection, the cells were harvested, and RNA was extracted using the RNeasy mini kit (Qiagen) for genome-wide sequencing. Down-regulation was made twice in four independent cells; two originated from apple-shaped women, and two originated from pear-shaped women. Transfection was validated by RT-qPCR as described by Roqueta-Rivera et al. (2016) (normalized by PPIA); a 76% average decrease in HOTAIR gene expression was found in the four subjects.

Chromatin immunoprecipitations

Chromatin immunoprecipitations (ChIPs) were performed and analyzed as described (Barish et al. 2012; Divoux et al. 2018). ChIP-grade Diagenode rabbit anti-H3K4me3 (C15410003), rabbit anti-H3K4me2 (pAb-035-050), rabbit anti-H3K27me3 (C15410 069), and Abcam rabbit anti-H3K27Ac (ab4729) were used to study the histone marks. CTCF antibody from Actif Motif (61311) was used to study CTCF boundary sites. Rabbit anti-RNAPII (ab5095) was used to study RNA polymerase II binding. Mouse

monoclonal anti-hnRNPA2B1 (Novus Biologicals NB120-6102SS) was used to study hnRNPA2B1 binding. The sequences of the oligos targeted to the specific genomic regions used in the study are listed in Supplemental Table S2.

Assay for transposase-accessible chromatin (ATAC)

ATAC was performed as previously described by Divoux et al. (2018).

Chromatin isolation by RNA purification (ChIRP)

ChIRP samples were prepared as described by Chu et al. (2012). Briefly, GF hASCs from one subject (healthy woman, apple-shaped, age 29 yr, BMI 35.9 kg/m^2) were grown until confluence. Six million cells were collected after trypsinization and centrifugation at 500*g* for 5 min. Cells were cross-linked with glutaraldehyde to preserve RNA–chromatin interactions before being lysed (50 mM Tris-Cl at pH 7.0, 10 mM EDTA, 1% SDS) and sonicated (1 h, 30 sec on, 45 sec off). Ten microliters of each probe specific to HOTAIR was added to the sample, and the fragmented chromatin associated with HOTAIR was pulled down using magnetic beads (Dynabeads Streptavidin, Invitrogen). A fraction of the sample was used for RNA extraction to validate HOTAIR pull-down by RT-qPCR as described by Roqueta-Rivera et al. (2016) using GAPDH as control (Supplemental Fig. S2C). The rest of the sample was used for DNA extraction as described by Chu et al. (2012) and sent to the Sanford-Burnham Prebys Genomics Core in Lake Nona, Florida, for sequencing. Antisense oligo probes were designed and ordered with BioSearch Technologies. The sequences of the 15 probes used in the study are listed in Supplemental Table S2, and their location within the HOTAIR sequence is shown in Supplemental Figure S2A.

Sequencing library preparation

RNA-seq, ATAC-seq, ChIRP-seq, and ChIP-seq libraries were prepared and sequenced using standard Illumina protocols for HiSeq 2500 instrument. hnRNPA2B1 ChIP-seq libraries were sequenced using standard Illumina protocols for NovaSeq PE150 platform.

RNA sequencing and analysis

RNA sequencing was performed as described (Divoux et al. 2018). The raw RNA-seq data were aligned to reference genome hg19 by using STAR (version 2.7.7a). Low-quality reads were filtered using SAMtools (version 1.3.1) view option with MAPQ <10 score. Duplicated reads and artifacts were removed using SAMtools -rmdup command, and then BEDTools (version 2.29.2) intersectBed option with hg19 consensus backlist. Transcript abundances were calculated using featureCounts from Rsubread (version 2.4.0). The R package edgeR (PMID: 27008025) with paired analysis was used for differential gene expression analysis with cutoffs cpm >2 for more than four samples. *P*-value <0.05 was used to determine statistical significance for differentially expressed genes.

The raw RNA-seq data of breast cancer and human epithelial kidney (HEK) cell lines were downloaded from Sequence Read Archive (SRA) data sets with the following numbers: SRR7789325–SRR7789330 (T47D control and silencing HOTAIR), SRR8429863–SRR8429866 (MCF-7 control and silencing HOTAIR), SRR6255390–SRR6255393 (HEK control and silencing HOTAIR) (Jarroux et al. 2021), SRR398237–SRR398238 (HEK93T control for hnRNPA2B1 silencing), and SRR398216–SRR398217 (HEK93T silencing hnRNPA2B1; PMID: 22574288). Differentially expressed genes were determined the same way as with our hASCs described above.

ChIP-seq and ATAC-seq analysis

Raw sequencing data were aligned to reference genome hg19 using Burrows–Wheeler alignment tool (BWA). Low-quality reads (MAPQ <10) and duplicated reads were filtered using SAMtools with "view" and "rmdup" options. Blacklist regions were removed using BEDTools. Blacklist regions were removed by using the intersectBed command in the BEDTools toolkit. A normalized bigwig file was generated using the bamCoverage command within the deepTools program.

hnRNPA2B1 and RNPAII RPKM values were calculated for each gene using the analyzeRepeat.pl Homer function.

ChIRP-seq analysis

Raw ChIRP-seq data were aligned to reference genome hg19 using Burrows–Wheeler alignment tool (BWA). Low-quality reads (MAPQ <30) and duplicated reads were filtered using SAMTools with the "view" and "rmdup" options. Blacklist regions were removed with the intersectBed command by using BEDtools. Peak calling was performed using MACS2. Reads per kilobase per million (RPKM) values were calculated on summits of ChIRP peaks with ±50-bp flanking regions by using coverageBed in the BEDtools toolset. Peaks with a minimum of eight RPKM were kept for further downstream analysis. A normalized bigwig file was generated using the bamCoverage command in the deepTools program. Annotation was performed using annotatePeaks.pl in HOMER. Genes with HOTAIR peaks were determined by intersection between gene body location (based on human GENCODE GRCh37) and HOTAIR ChIRP peaks by using intersectBed in BEDTools. The top 5000 protein-coding genes were selected for gene set enrichment analysis based on the RPKM of the overlapping HOTAIR peaks.

Motif analysis

Motif enrichment analysis within HOTAIR ChIRP peaks was carried out by findMotifsGenome.pl (HOMER). It was performed on the ±100-bp flanking regions of the top 10,000 ChIRP peak summits based on reads per kilobase per million (RPKM). Motif enrichment analysis within the promoters of differentially expressed genes after HOTAIR silencing in GF hASCs overlapped with or without HOTAIR ChIRP peaks was performed by findMotifs.pl (HOMER) with −1.25 kb and +0.25 kb from TSS promoter options.

Gene set enrichment and visualization

HypeR, an R package, was used for gene set enrichment and visualization (Federico and Monti 2020). The enrichment was calculated to the Hallmark gene set of Molecular Signature Database (MsigDb). Significant pathways with *P*-value <0.05 were selected.

ChromHMM

Chromatin states were learned jointly by applying the ChromHMM (version 1.21) hidden Markov model (HMM) algorithm at 200-bp resolution to seven data tracks (RNAPII, CTCF, ATAC, H3K27ac, H3K27me3, H3K4me2, and H3K4me3) from each of the four ABD hASC and four GF hASC samples, as previously described (Ernst et al. 2011). We ran ChromHMM with a

range of possible states and settled on a 10-state model, as it accurately captured information from higher-state models and provided sufficient resolution to identify biologically meaningful patterns in a reproducible way (Ernst and Kellis 2017).

Metagene profiles

To show the normalized signals of HOTAIR, RNAPII, H3K27me3, and H3K4me2 around full gene bodies with and without HOTAIR ChIRP peaks, metagene profile was used by the computeMatrix -scale-regions option in the deepTools program. Genes with neighboring genes that overlapped within 7 kb downstream from the TES regions of our differently expressed genes were excluded. Calculated normalized signals were derived from bamCoverage (deepTools) using reads per genome coverage (RPGC).

For statistical analysis, differentially expressed genes were grouped by those with or without HOTAIR binding (overlapped with any regions of gene body) sites. For these genes, TSS regions were defined as TSSs with ±500-bp flanking regions, and TES regions were defined as TESs with ±1000-bp flanking regions. Signals of each factor (HOTAIR, RNAPII, H3K27me3, and H3K4me2) at TSSs and TESs were calculated by using computeMatrix-scale-regions. Signal values were exported as a table by using Profileplyr, an R package with a summarize function by rowMeans. Statistical significance of differences was assessed using unpaired two-sample Wilcoxon test.

To group all human genes by gene expression level, RNA-seq derived from control GF hASCs of four subjects was used. Protein-coding and lncRNA genes were included in the analysis based on human GENCODE GRCh37. Transcripts per million (TPM) values were calculated by using TPMCalculator (Vera Alvarez et al. 2019). Average TPM of four subjects was calculated and ranked. TPM values equal to zero were excluded. Based on data distribution, first quartile of data means the "low" (0%–25%), interquartile range (25%–75%) means the "medium," and third quartile (75%–100%) means "high" expression level. RPKM values of HOTAIR peaks overlapping with genes were compared between each expression group.

RNA–RNA interactions

Previously published data were used to investigate RNA–RNA interactions between HOTAIR lncRNA and full transcriptome (Terai et al. 2016). Minimum energy of −24.5 kcal/mol or greater was used as a cutoff, resulting in 12,719 interactions. Data contained the gene names, gene location, location of the RNA–RNA interactions on the transcripts, binding sites with RNA on HOTAIR sequence, minimum energy (MinEnergy), and sum of the energy (SumEnergy). Genes were grouped by the presence (+HOT) or absence (−HOT) of HOTAIR ChIRP peaks on the gene body.

Visualization and statistics

To plot the heat map of ChIRP-seq signals and histograms of ChIP-seq and ChIRP-seq signals, we used the plotHeatmap and plotProfile commands in deepTools (version 3.5.1) (Ramírez et al. 2014). Most of the plots were created using different packages in R, listed here. Volcano plots were created using EnhancedVolcano, an R package (https://bioconductor.org/packages/devel/bioc/vignettes/EnhancedVolcano/inst/doc/EnhancedVolcano.html). To plot heat maps of gene expression and pathways for ChIRP-seq data, we used the ComplexHeatmap package (Gu et al. 2016). ChromHMM heat maps were generated using EnrichedHeatmap (Gu et al. 2018). The Profileplyr, R package was used to visualize the heat map for ChIRP peaks with the AATAAA motif (https://www.bioconductor.org/packages/release/bioc/html/profileplyr.html).

Box plots, bar graphs, and histograms were created using the ggplot2 and the ggpubr package. To visualize the intersection of differentially expressed genes, the UpSetR package was used.

To determine the statistical significance, ggpubr was used. To compare two independent groups, we used unpaired two-sample Wilcoxon test (Wilcoxon rank sum test). To compare paired data, we used paired-sample Wilcoxon test (Wilcoxon signed rank test).

Trial registration

This study is registered at ClinicalTrials.gov (NCT02728635; retrospectively registered March 24, 2016; https://clinicaltrials.gov/ct2/show/NCT02728635).

Ethics and consent

This study was approved by the AdventHealth Institutional Review Board. All participants provided written and informed consent before screening and participation in the study.

Availability of data

All sequencing data have been deposited to the NCBI GEO database (http://www.ncbi.nlm.nih.gov/geo) under accession numbers GSE 192749, GSE 192750, and GSE 201597.

Competing interest statement

The authors declare no competing interests.

Acknowledgments

We thank the study volunteers for their participation, and the Translational Research Institute (TRI)-MD clinical research staff for their contributions. We thank the personnel of the Genomic Cores at Sanford-Burnham Prebys Medical Discovery Institute, Orlando, FL (particularly John Marchica), and Johns Hopkins University who performed the sequencing; and Crystal Young-Erdos for her help with text editing. This study was funded by National Institutes of Health grant R01DK107009-02.

Author contributions: E.E. conceived and visualized the study; performed the methodology, investigation, and formal analysis; was responsible for the software; and reviewed and edited the manuscript. A.D. conceived the study; performed the methodology; investigation, and formal analysis; and wrote the original draft of the manuscript. K.S. performed the methodology and investigation, and reviewed and edited the manuscript. L.H. performed the formal analysis, was responsible for the software, and reviewed and edited the manuscript. S.R.S. conceived and supervised the study, acquired funding, and reviewed and edited the manuscript. T.F.O. conceived and supervised the study, performed the methodology, acquired funding, and reviewed and edited the manuscript.

References

Anveden Å, Sjöholm K, Jacobson P, Palsdottir V, Walley AJ, Froguel P, Al-Daghri N, McTernan PG, Mejhert N, Arner P, et al. 2012. ITIH-5 expression in human adipose tissue is increased in obesity. *Obesity* **20:** 708–714. doi:10.1038/oby.2011.268

Baglioni S, Cantini G, Poli G, Francalanci M, Squecco R, Di Franco A, Borgogni E, Frontera S, Nesi G, Liotta F, et al. 2012. Functional differences in visceral and subcutaneous fat pads originate from differences in the adipose stem cell. *PloS one* **7:** e36569. doi:10.1371/journal.pone.0036569

Balas MM, Hartwick EW, Barrington C, Roberts JT, Wu SK, Bettcher R, Griffin AM, Kieft JS, Johnson AM. 2021. Establishing RNA–RNA interactions remodels lncRNA structure and promotes PRC2 activity. *Sci Adv* **7:** eabc9191. doi:10.1126/sciadv.abc9191

Barish GD, Yu RT, Karunasiri MS, Becerra D, Kim J, Tseng TW, Tai LJ, Leblanc M, Diehl C, Cerchietti L, et al. 2012. The Bcl6–SMRT/NCoR cistrome represses inflammation to attenuate atherosclerosis. *Cell Metab* **15:** 554–562. doi:10.1016/j.cmet.2012.02.012

Boney CM, Moats-Staats BM, Stiles AD, D'Ercole AJ. 1994. Expression of insulin-like growth factor-I (IGF-I) and IGF-binding proteins during adipogenesis. *Endocrinology* **135:** 1863–1868. doi:10.1210/endo.135.5.7525256

Boyle KB, Hadaschik D, Virtue S, Cawthorn WP, Ridley SH, O'Rahilly S, Siddle K. 2009. The transcription factors Egr1 and Egr2 have opposing influences on adipocyte differentiation. *Cell Death Differ* **16:** 782–789. doi:10.1038/cdd.2009.11

Bure I, Geer S, Knopf J, Roas M, Henze S, Ströbel P, Agaimy A, Wiemann S, Hoheisel JD, Hartmann A, et al. 2018. Long noncoding RNA *HOTAIR* is upregulated in an aggressive subgroup of gastrointestinal stromal tumors (GIST) and mediates the establishment of gene-specific DNA methylation patterns. *Genes Chromosomes Cancer* **57:** 584–597. doi:10.1002/gcc.22672

Cheng D, Deng J, Zhang B, He X, Meng Z, Li G, Ye H, Zheng S, Wei L, Deng X, et al. 2018. LncRNA HOTAIR epigenetically suppresses miR-122 expression in hepatocellular carcinoma via DNA methylation. *EBioMedicine* **36:** 159–170. doi:10.1016/j.ebiom.2018.08.055

Chu C, Qu K, Zhong FL, Artandi SE, Chang HY. 2011. Genomic maps of long noncoding RNA occupancy reveal principles of RNA–chromatin interactions. *Mol Cell* **44:** 667–678. doi:10.1016/j.molcel.2011.08.027

Chu C, Quinn J, Chang HY. 2012. Chromatin isolation by RNA purification (ChIRP). *J Vis Exp* **61:** 3912. doi:10.3791/3912

Denton N, Pinnick KE, Karpe F. 2018. Cartilage oligomeric matrix protein is differentially expressed in human subcutaneous adipose tissue and regulates adipogenesis. *Mol Metab* **16:** 172–179. doi:10.1016/j.molmet.2018.07.005

Divoux A, Karastergiou K, Xie H, Guo W, Perera RJ, Fried SK, Smith SR. 2014. Identification of a novel lncRNA in gluteal adipose tissue and evidence for its positive effect on preadipocyte differentiation. *Obesity* **22:** 1781–1785. doi:10.1002/oby.20793

Divoux A, Sandor K, Bojcsuk D, Talukder A, Li X, Balint BL, Osborne TF, Smith SR. 2018. Differential open chromatin profile and transcriptomic signature define depot-specific human subcutaneous preadipocytes: primary outcomes. *Clin Epigenetics* **10:** 148. doi:10.1186/s13148-018-0582-0

Divoux A, Sandor K, Bojcsuk D, Yi F, Hopf ME, Smith JS, Balint BL, Osborne TF, Smith SR. 2020. Fat distribution in women is associated with depot-specific transcriptomic signatures and chromatin structure. *J Endocr Soc* **4:** bvaa042. doi:10.1210/jendso/bvaa042

Divoux A, Eroshkin A, Erdos E, Sandor K, Osborne TF, Smith SR. 2021. DNA methylation as a marker of body shape in premenopausal women. *Front Genet* **12:** 709342. doi:10.3389/fgene.2021.709342

Duclos M. 2016. Osteoarthritis, obesity and type 2 diabetes: the weight of waist circumference. *Ann Phys Rehabil Med* **59:** 157–160. doi:10.1016/j.rehab.2016.04.002

Eguchi J, Yan QW, Schones DE, Kamal M, Hsu CH, Zhang MQ, Crawford GE, Rosen ED. 2008. Interferon regulatory factors are transcriptional regulators of adipogenesis. *Cell Metab* **7:** 86–94. doi:10.1016/j.cmet.2007.11.002

Ernst J, Kellis M. 2017. Chromatin-state discovery and genome annotation with ChromHMM. *Nat Protoc* **12:** 2478–2492. doi:10.1038/nprot.2017.124

Ernst J, Kheradpour P, Mikkelsen TS, Shoresh N, Ward LD, Epstein CB, Zhang X, Wang L, Issner R, Coyne M, et al. 2011. Mapping and analysis of chromatin state dynamics in nine human cell types. *Nature* **473:** 43–49. doi:10.1038/nature09906

Farmer SR. 2006. Transcriptional control of adipocyte formation. *Cell Metab* **4:** 263–273. doi:10.1016/j.cmet.2006.07.001

Federico A, Monti S. 2020. Hyper: an R package for geneset enrichment workflows. *Bioinformatics* **36:** 1307–1308. doi:10.1093/bioinformatics/btz700

Gealekman O, Gurav K, Chouinard M, Straubhaar J, Thompson M, Malkani S, Hartigan C, Corvera S. 2014. Control of adipose tissue expandability in response to high fat diet by the insulin-like growth factor-binding protein-4. *J Biol Chem* **289:** 18327–18338. doi:10.1074/jbc.M113.545798

Gencer S, Döring Y, Jansen Y, Bayasgalan S, Schengel O, Müller M, Peters LJF, Weber C, van der Vorst EPC. 2021. Adipocyte-specific ACKR3 regulates lipid levels in adipose tissue. *Biomedicines* **9:** 394. doi:10.3390/biomedicines9040394

Goedecke JH, Levitt NS, Lambert EV, Utzschneider KM, Faulenbach MV, Dave JA, West S, Victor H, Evans J, Olsson T, et al. 2009. Differential effects of abdominal adipose tissue distribution on insulin sensitivity in black and white South African women. *Obesity* **17:** 1506–1512. doi:10.1038/oby.2009.73

Goodpaster BH, Thaete FL, Simoneau JA, Kelley DE. 1997. Subcutaneous abdominal fat and thigh muscle composition predict insulin sensitivity independently of visceral fat. *Diabetes* **46:** 1579–1585. doi:10.2337/diacare.46.10.1579

Gu Z, Eils R, Schlesner M. 2016. Complex heatmaps reveal patterns and correlations in multidimensional genomic data. *Bioinformatics* **32:** 2847–2849. doi:10.1093/bioinformatics/btw313

Gu Z, Eils R, Schlesner M, Ishaque N. 2018. Enrichedheatmap: an R/Bioconductor package for comprehensive visualization of genomic signal associations. *BMC Genomics* **19:** 234. doi:10.1186/s12864-018-4625-x

Gupta RA, Shah N, Wang KC, Kim J, Horlings HM, Wong DJ, Tsai MC, Hung T, Argani P, Rinn JL, et al. 2010. Long non-coding RNA HOTAIR reprograms chromatin state to promote cancer metastasis. *Nature* **464:** 1071–1076. doi:10.1038/nature08975

Hajjari M, Salavaty A. 2015. HOTAIR: an oncogenic long noncoding RNA in different cancers. *Cancer Biol Med* **12:** 1–9. doi:10.7497/j.issn.2095-3941.2015.0006

Huelga SC, Vu AQ, Arnold JD, Liang TY, Liu PP, Yan BY, Donohue JP, Shiue L, Hoon S, Brenner S, et al. 2012. Integrative genome-wide analysis reveals cooperative regulation of alternative splicing by hnRNP proteins. *Cell Rep* **1:** 167–178. doi:10.1016/j.celrep.2012.02.001

Isacco L, Ennequin G, Boisseau N. 2021. Influence of the different hormonal status changes during their life on fat mass localisation in women: a narrative review. *Arch Physiol Biochem* doi:10.1080/13813455.2021.1933045

Jarroux J, Foretek D, Bertrand C, Gabriel M, Szachnowski U, Saci Z, Guo S, Londoño-Vallejo A, Pinskaya M, Morillon A. 2021. HOTAIR lncRNA promotes epithelial–mesenchymal

transition by redistributing LSD1 at regulatory chromatin regions. *EMBO Rep* **22:** e50193. doi:10.15252/embr.202050193

Jia R, Li T, Wang N. 2021. Long noncoding RNA HOTAIR functions as ceRNA to regulate MMP2 in paraquat induced lung epithelial–mesenchymal transition. *Toxicology* **461:** 152891. doi:10.1016/j.tox.2021.152891

Karastergiou K, Fried SK, Xie H, Lee MJ, Divoux A, Rosencrantz MA, Chang RJ, Smith SR. 2013. Distinct developmental signatures of human abdominal and gluteal subcutaneous adipose tissue depots. *J Clin Endocrinol Metab* **98:** 362–371. doi:10.1210/jc.2012-2953

Lee JE, Schmidt H, Lai B, Ge K. 2019. Transcriptional and epigenomic regulation of adipogenesis. *Mol Cell Biol* **39:** e00601-18. doi:10.1128/MCB.00601-18

Li S, Xiong Q, Chen M, Wang B, Yang X, Yang M, Wang Q, Cui Z, Ge F. 2021. Long noncoding RNA HOTAIR interacts with Y-box protein-1 (YBX1) to regulate cell proliferation. *Life Sci Alliance* **4:** e202101139. doi:10.26508/lsa.202101139

Liu XH, Sun M, Nie FQ, Ge YB, Zhang EB, Yin DD, Kong R, Xia R, Lu KH, Li JH, et al. 2014. Lnc RNA HOTAIR functions as a competing endogenous RNA to regulate HER2 expression by sponging miR-331-3p in gastric cancer. *Mol Cancer* **13:** 92. doi:10.1186/1476-4598-13-92

Lu MY, Liao YW, Chen PY, Hsieh PL, Fang CY, Wu CY, Yen ML, Peng BY, Wang DP, Cheng HC, et al. 2017. Targeting LncRNA HOTAIR suppresses cancer stemness and metastasis in oral carcinomas stem cells through modulation of EMT. *Oncotarget* **8:** 98542–98552. doi:10.18632/oncotarget.21614

Manolopoulos KN, Karpe F, Frayn KN. 2010. Gluteofemoral body fat as a determinant of metabolic health. *Int J Obes* **34:** 949–959. doi:10.1038/ijo.2009.286

Meredith EK, Balas MM, Sindy K, Haislop K, Johnson AM. 2016. An RNA matchmaker protein regulates the activity of the long noncoding RNA HOTAIR. *RNA* **22:** 995–1010. doi:10.1261/rna.055830.115

Merrick D, Sakers A, Irgebay Z, Okada C, Calvert C, Morley MP, Percec I, Seale P. 2019. Identification of a mesenchymal progenitor cell hierarchy in adipose tissue. *Science* **364:** eaav2501. doi:10.1126/science.aav2501

Mor-Yossef Moldovan L, Lustig M, Naftaly A, Mardamshina M, Geiger T, Gefen A, Benayahu D. 2019. Cell shape alteration during adipogenesis is associated with coordinated matrix cues. *J Cell Physiol* **234:** 3850–3863. doi:10.1002/jcp.27157

Morrison RF, Farmer SR. 1999. Insights into the transcriptional control of adipocyte differentiation. *J Cell Biochem* **Suppl 32–33:** 59–67. doi:10.1002/(SICI)1097-4644(1999)75:32+<59::AID-JCB8>3.0.CO;2-1

Mozdarani H, Ezzatizadeh V, Rahbar Parvaneh R. 2020. The emerging role of the long non-coding RNA HOTAIR in breast cancer development and treatment. *J Transl Med* **18:** 152. doi:10.1186/s12967-020-02320-0

Nishimura S, Nagasaki M, Okudaira S, Aoki J, Ohmori T, Ohkawa R, Nakamura K, Igarashi K, Yamashita H, Eto K, et al. 2014. ENPP2 contributes to adipose tissue expansion and insulin resistance in diet-induced obesity. *Diabetes* **63:** 4154–4164. doi:10.2337/db13-1694

Pan SC, Cui HH, Qiu CG. 2018. HOTAIR promotes myocardial fibrosis through regulating URI1 expression via Wnt pathway. *Eur Rev Med Pharmacol Sci* **22:** 6983–6990.

Passaro A, Miselli MA, Sanz JM, Dalla Nora E, Morieri ML, Colonna R, Pišot R, Zuliani G. 2017. Gene expression regional differences in human subcutaneous adipose tissue. *BMC Genomics* **18:** 202. doi:10.1186/s12864-017-3564-2

Pinnick KE, Nicholson G, Manolopoulos KN, McQuaid SE, Valet P, Frayn KN, Denton N, Min JL, Zondervan KT, Fleckner J, et al. 2014. Distinct developmental profile of lower-body adipose tissue defines resistance against obesity-associated metabolic complications. *Diabetes* **63:** 3785–3797. doi:10.2337/db14-0385

Qu X, Alsager S, Zhuo Y, Shan B. 2019. HOX transcript antisense RNA (HOTAIR) in cancer. *Cancer Lett* **454:** 90–97. doi:10.1016/j.canlet.2019.04.016

Ramírez F, Dündar F, Diehl S, Grüning BA, Manke T. 2014. Deeptools: a flexible platform for exploring deep-sequencing data. *Nucleic Acids Res* **42:** W187–W191. doi:10.1093/nar/gku365

Roqueta-Rivera M, Esquejo RM, Phelan PE, Sandor K, Daniel B, Foufelle F, Ding J, Li X, Khorasanizadeh S, Osborne TF. 2016. SETDB2 links glucocorticoid to lipid metabolism through Insig2a regulation. *Cell Metab* **24:** 474–484. doi:10.1016/j.cmet.2016.07.025

Rosen ED, MacDougald OA. 2006. Adipocyte differentiation from the inside out. *Nat Rev Mol Cell Biol* **7:** 885–896. doi:10.1038/nrm2066

Rosen ED, Spiegelman BM. 2000. Molecular regulation of adipogenesis. *Annu Rev Cell Dev Biol* **16:** 145–171. doi:10.1146/annurev.cellbio.16.1.145

Sánchez-Solana B, Laborda J, Baladrón V. 2012. Mouse resistin modulates adipogenesis and glucose uptake in 3T3-L1 preadipocytes through the ROR1 receptor. *Mol Endocrinol* **26:** 110–127. doi:10.1210/me.2011-1027

Shi C, Huang F, Gu X, Zhang M, Wen J, Wang X, You L, Cui X, Ji C, Guo X. 2016. Adipogenic miRNA and meta-signature miRNAs involved in human adipocyte differentiation and obesity. *Oncotarget* **7:** 40830–40845. doi:10.18632/oncotarget.8518

Squillaro T, Peluso G, Galderisi U, Di Bernardo G. 2020. Long non-coding RNAs in regulation of adipogenesis and adipose tissue function. *Elife* **9:** e59053. doi:10.7554/eLife.59053

Tang Y, Song G, Liu H, Yang S, Yu X, Shi L. 2021. Silencing of long non-coding RNA HOTAIR alleviates epithelial–mesenchymal transition in pancreatic cancer via the Wnt/β-catenin signaling pathway. *Cancer Manag Res* **13:** 3247–3257. doi:10.2147/CMAR.S265578

Terai G, Iwakiri J, Kameda T, Hamada M, Asai K. 2016. Comprehensive prediction of lncRNA–RNA interactions in human transcriptome. *BMC Genomics* **17 Suppl 1:** 12. doi:10.1186/s12864-015-2307-5

Topel H, Bagirsakci E, Comez D, Bagci G, Cakan-Akdogan G, Atabey N. 2020. lncRNA HOTAIR overexpression induced downregulation of c-Met signaling promotes hybrid epithelial/mesenchymal phenotype in hepatocellular carcinoma cells. *Cell Commun Signal* **18:** 110. doi:10.1186/s12964-020-00602-0

Tsai MC, Manor O, Wan Y, Mosammaparast N, Wang JK, Lan F, Shi Y, Segal E, Chang HY. 2010. Long noncoding RNA as modular scaffold of histone modification complexes. *Science* **329:** 689–693. doi:10.1126/science.1192002

Tzanavari T, Giannogonas P, Karalis KP. 2010. TNF-α and obesity. *Curr Dir Autoimmun* **11:** 145–156. doi:10.1159/000289203

Vera Alvarez R, Pongor LS, Mariño-Ramírez L, Landsman D. 2019. TPMCalculator: one-step software to quantify mRNA abundance of genomic features. *Bioinformatics* **35:** 1960–1962. doi:10.1093/bioinformatics/bty896

Wang Y, Yi K, Liu X, Tan Y, Jin W, Li Y, Zhou J, Wang H, Kang C. 2021. HOTAIR up-regulation activates NF-κB to induce immunoescape in gliomas. *Front Immunol* **12:** 785463. doi:10.3389/fimmu.2021.785463